Nanoscale Advances

ROYAL SOCIETY OF CHEMISTRY

PAPER

View Article Online
View Journal | View Issue

Cite this: *Nanoscale Adv.*, 2024, **6**, 4237

Coalescence behavior of size-selected gold and tantalum nanoclusters under electron beam irradiation: insights into nano-welding mechanisms

Shengyong Hu, †[ab] Syed Adil Shah, †[c] Syed Niaz Ali Shah, [d] Zixiang Zhao,[ab] Wuwen Zhu,[ab] Yongxin Zhang,[ab] Siqi Lu,[ab] Sichen Tang,[ab] Kuo-Juei Hu *[ab] and Fengqi Song *[ab]

The emerging technique of nano-welding (NW) *via* precisely regulating the fusion of nanoclusters (NCs) in nanotechnology has attracted significant attention for its innovative approach. Employing the gas-phase condensation cluster source with a lateral time-of-flight (TOF) mass-selector, size-selected gold (Au), and tantalum (Ta) NCs were prepared. This study explores the coalescence behavior of size-selected Au and Ta NCs under electron beam irradiation, aiming to investigate the related mechanism governing the welding process. Intrinsically driven by the reduction of excess surface energy, electron beam induces atomic thermal migration, fostering sintering neck growth at cluster interfaces. During this process, atomic diffusion and recrystallization enable NCs to alter shape while retaining stable facet planes. Aberration-corrected scanning transmission electron microscopy (AC-STEM) showcases the formation of single or polycrystalline sintered clusters, during which some lattice distortions can be eliminated. Interestingly, oxidized Ta clusters experience knock-on damage caused by elastic scattering of electron beams, partially deoxidizing them. Additionally, electron–phonon inelastic scattering transforms oxidized Ta clusters from amorphous to crystalline structures. Moreover, the quantum size effect and surface effect of NCs facilitate the surpassing of miscibility limits during Au–Ta heterogeneous welding processes. This investigation bridges the gap between fundamental research on cluster materials and their practical applications.

Received 5th May 2024
Accepted 3rd July 2024

DOI: 10.1039/d4na00373j

rsc.li/nanoscale-advances

Introduction

In the dynamic landscape of nanotechnology, the manipulation and fusion of nanoclusters (NCs) at the atomic level opens up a realm of possibilities for advanced materials and applications.[1,2] Among the myriad advancements in this field, nano-welding (NW) stands out as a ground-breaking technique, enabling the controlled merging of individual NCs into larger structures under precise conditions.[3–5] Also known as nanoparticle coalescence, this process represents a paradigm shift in nanotechnology, driven by the application of external stimuli, such as electron beams, which provide the necessary energy to break and reform atomic bonds at the nanoscale.[6,7] Gold (Au) and tantalum (Ta) NCs have emerged as prominent candidates for NW experiments, owing to their distinctive electronic and structural properties. Au is renowned for its exceptional conductivity and stability finds applications in a wide array of fields including electronics, catalysis, and medical diagnostics.[8–10] Conversely, Ta boasts remarkable thermal stability and corrosion resistance, positioning it as a cornerstone for high-performance alloys and electronics components.[11,12] Superalloys and refractory metals are widely used in aerospace, national defense, and other fields due to their excellent properties.[13,14] Because of the rapid pace of technological progress, the working temperatures of specialty metal materials have increased recently, which has made their welding techniques more complex.[15] The strict requirements on performance and service life associated with welding applications are gradually posing challenges for conventional welding procedures, such as brazing, pressure welding, and fusion welding.[16]

Electron beam welding (EBW) is an advanced technology that utilizes high-energy electron irradiation to rapidly melt the materials in the welding area, effectively converting the kinetic energy of electrons into thermal energy.[17,18] Compared to traditional welding methods, EBW offers advantages such as

[a]*National Laboratory of Solid State Microstructures, Collaborative Innovation Center of Advanced Microstructures, School of Physics, Nanjing University, Nanjing 210093, China. E-mail: kuojueihu@nju.edu.cn; songfengqi@nju.edu.cn*

[b]*Institute of Atom Manufacturing, Nanjing University, Suzhou Campus, Nanjing 215163, People's Republic of China*

[c]*School of Biomedical Engineering, Health Science Centre, Shenzhen University Shenzhen, Guangdong 518060, PR China*

[d]*Innovation and Technology Transfer, King Fahd University of Petroleum and Minerals, Dhahran 31261, Saudi Arabia*

† These authors contributed equally to this work.

high-power density, high processing accuracy, large depth-to-width ratio of welds, minimal welding deformation, excellent technology adaptability, good repeatability, reproducibility, and minimal contamination in vacuum environments. Therefore, it has been widely used in welding superalloys, refractory metals, and intermetallic compounds.[17,19,20] During electron beam irradiation (EBI), the transfer of kinetic energy to the NCs induces localized heating, leading to the diffusion of surface atoms across the surfaces.[6,19,21,22] This phenomenon initiates the formation of necks between adjacent NCs, which gradually evolve into robust bonds under prolonged irradiation.

The EBW between homogeneous metals and miscible metals is relatively easier to achieve.[23] However, challenges still exist in EBW between many immiscible materials.[24,25] Taking advantage of the high energy density and low heat stress characteristics of EBW, overcoming issues such as welding cracks and metallurgical incompatibilities caused by differences in thermal and chemical properties between immiscible materials is a current research focus in the field of dissimilar materials welding.[26,27] Metal clusters possess characteristics such as larger specific surface area, higher surface energy, and smaller curvature radius, making surface atoms of metal clusters highly prone to thermal migration.[28] Moreover, their melting points are much lower than those of bulk materials, with some clusters capable of sintering at relatively low or even room temperature.[12,29] Reinvigorated by this, it is possible to decrease the melting point of metal materials without altering their elemental composition. In the EBW process of immiscible materials, the two types of clusters corresponding to the base materials can be used as intermediate fillers between the weld joints. Clusters can sinter at temperatures much lower than the melting point of bulk materials.[5,22,30] Additionally, the quantum size effect and surface effect of clusters allow them to surpass the mixing limits of bulk materials.[31] This results in superior mechanical and electrical properties after welding,[32] ultimately achieving the ideal combination of low-temperature processing and high-temperature performance.[33]

With advancements in electron microscopy, individuals can observe and manipulate in real-time, allowing for a comprehensive exploration of the intricacies at nano and even atomic scales.[34] However, research on the *in situ* characterization of cluster welding processes under EBI and the intrinsic mechanisms of EBW remains limited.[35,36] While the preparation, characterization, and performance studies of cluster materials have become increasingly mature, the atomic manufacturing technology used to assemble them into functional nanodevices is still in its infancy.[37,38] The NW is a vital step towards bottom-up atomic manufacturing, facilitating the transition of cluster material research from laboratory experiments to large-scale practical applications.[39,40] It represents a frontier direction in the current and foreseeable future of nanotechnology. The advancement of NW will pave the way for various cutting-edge applications such as 3D nano printing, the connection of nanodevice units, high-temperature power chip packaging, *etc.*[41–46] This study investigates the EBW of size-selected Au and Ta clusters based on *in situ* AC-STEM. We observed the homogeneous and heterogeneous welding process of clusters at atomic resolution and revealed the intrinsic mechanisms involved in EBW to explain the observed phenomena. Understanding the coalescence mechanism of Au and Ta NCs during the NW process enhances our comprehension of nanomaterials and paves the way for tailored materials engineering across a spectrum of applications, from electronics to catalysis and beyond.

Experimental

Materials

A Ta target (purity > 99.99%) and an Au target (purity > 99.999%), both with a diameter of 76.2 mm, were procured from Hebei Qinbang New Material Technology Co., Ltd for DC magnetron-sputtering targets. Pure carbon film-coated grids from Nanjing Zhongjingkeyi Technology Co., Ltd were used as substrates for STEM characterization.

Sample preparation

Our laboratory employed a cluster beam source that consists of a magnetron-sputtering and gas-phase condensation chamber, ion optics, a time-of-flight (TOF) mass-selector, and a deposition chamber. This setup can produce clusters ranging in size from 2 atoms up to at least 20 000 atoms, depending on the target material. This apparatus boasts a resolution of $R = m/\Delta m \geq 20$, enabling the generation of nanoclusters with a precision of $\pm 2.5\%$ in terms of the number of atoms per cluster. And it is designed to match various operational requirements such as vacuum conditions, power supply, cooling system, current detection, and control procedures. Additionally, the deposition chamber is equipped with a simple Faraday cup setup for cluster collection while using a Pico ammeter (Keithley 6485) to measure the rate of cluster deposition.

Size-selected Au and Ta NCs are generated using the cluster beam source described above, and the as-deposited clusters are studied by AC-STEM. In addition, all clusters were deposited onto the substrates using a soft-landing technique, ensuring the deposition energy (E_k) is below 1 eV per atom. This method effectively preserves the clusters' original structure and prevents additional interactions between the clusters and substrates.

Characterization

The high-angle annular dark field (HAADF) images were acquired using spherical aberration-corrected electron microscopy (200 kV FEI Themis Z) at the National Graphene Products Quality Inspection and Testing Center in Wuxi, China. The image data processing was performed using Velox, ImageJ, and Digital Micrograph software.

The screen current used in high-resolution HAADF-STEM imaging was set to 62 pA, while the current used in energy-dispersive X-ray spectroscopy (EDS) characterization was set to 210 pA. The electron dose in STEM mode can be calculated using the following formula:

$$\text{Electron dose}\left(\text{e}^{-}\ \text{per nm}^2\ \text{per frame}\right) = \frac{\text{screen current(A)} \times \text{frame time(s)}}{\text{charge } e^{-}\text{(C)} \times \text{frame area(mm}^2\text{)}}$$

Results and discussion

Homogeneous EBW between Au NCs

The EBW process between two Au_{2057} clusters is depicted in Fig. 1, showcasing the evolution of a neck formation. It was performed with an electron dose of 1.55×10^7 e^- per nm^2 per frame. Initially, a narrow neck spanning only 2 atomic layers emerged, marked by the blue and orange lines connecting the cluster centers to the neck center forming an angle of 159°. Intrinsically driven by the reduction of excess surface energy, the neck widened to 4 atomic layers, with the angle between the lines expanding to 170° after 60 seconds of EBI. Subsequently, between $t = 60$–120 s, rapid neck enlargement ensued, accompanied by automatic lattice matching, resulting in the formation of a peanut-like configuration with the angle reaching 180°. Notably, their relative crystallographic orientations do not match, the grain boundaries (yellow dashed lines depicted in Fig. 1) were formed at the cluster–cluster interface. To reduce the thermodynamically non-negligible interface energy of the boundaries, dislocation slipped along the (111) crystal, advancing layer by layer. In addition, there was competition in the orientation of atomic structures within the clusters. The *d*-spacing between the (111) crystal planes, measured to be 2.466 Å, is slightly larger than the value (2.3548 Å) mentioned in the JCPDS PDF data #98-000-0230. As the irradiation time increased, the two Au_{2057} clusters progressively merged, gradually filling in the necked areas. After 540 seconds of EBI, a face-centered cubic (FCC) structure was formed as indicated by the fast Fourier transform (FFT) power spectrum along the [110] zone axis (inset Fig. 1). A significant trailing phenomenon in the FFT pattern was observed, indicating the presence of stacking faults within the cluster.

Fig. 2 illustrates the EBW process of another pair of Au_{2057} clusters with an electron dose of 7.83×10^6 e^- per nm^2 per frame. Initially, the two Au_{2057} clusters were relatively far apart with a separation distance of about 1 nm, resulting in a higher energy barrier for this welding process. Due to the intensified thermal migration of surface atoms induced by EBI, protrusions emerged on the cluster surfaces after 120 seconds at locations indicated by the yellow arrows, which served as precursors to neck formation. The subsequent process is analogous to that depicted in Fig. 1, where atom-by-atom reorientation *via* dislocation and grain boundary migration occurred. This resulted in the formation of an FCC-twinned structure after 720 seconds of EBI, with the twinned boundary indicated by the yellow arrows. FFT analysis indicates that the crystallographic zone axes of both clusters are along the [211] axis. The reciprocal space spot pattern corresponding to the crystal planes of the left and right Au_{2057} clusters are marked in blue and green, respectively. The $(\bar{1}\bar{1}3)$ and $(11\bar{3})$ crystal planes of the left cluster overlap with the $(\bar{1}3\bar{1})$ and $(1\bar{3}1)$ crystal planes of the right cluster. After 5760 seconds of EBI, sufficient coalescence and structural relaxation occurred during the welding process of two Au_{2057} clusters, resulting in a more spherical shape that significantly reduced the overall surface energy. The corresponding FFT analysis indicates the formation of FCC polycrystalline structure along the [110] zone axis.

Some similar EBI was performed on other Au clusters, revealing that the features of the welding processes were essentially the same. The coalescence of clusters in the electron beam NW process is intrinsically driven by the reduction of total surface energy of the entire system. EBI serves as an external stimulus, transferring energy from the electron beam to the specimen and inducing a Brownian-like motion. Consequently, the initial metastable state of the system was disrupted, leading to electron beam-driven surface atoms migration, which governs the coalescence behavior of clusters. Herein, we present real-time observation of the neck formation, oriented attachment, and structural relaxation in the electron beam NW process of Au_{2057} clusters. The neck is unstable due to its high curvature, surface atoms with low coordination gradually diffuse to the cluster interface, filling the high-curvature neck

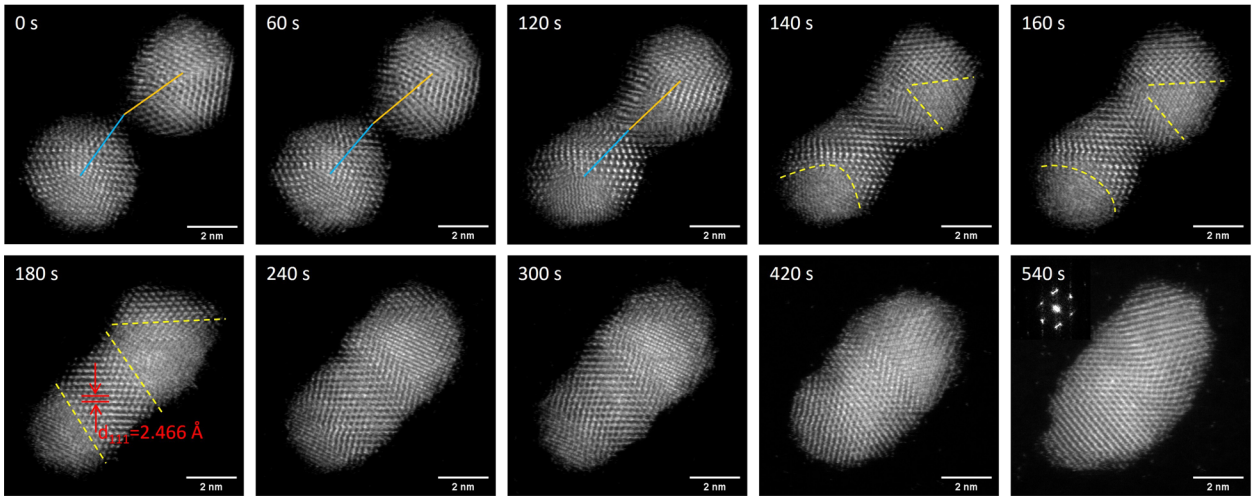

Fig. 1 Real-time sequential HAADF-STEM images of the coalescence process of Au_{2057} clusters under electron beam irradiation. The blue and orange lines connect the center of Au_{2057} clusters to the center of the neck, while the yellow dashed lines represent grain boundaries. The inset at 540 s shows the corresponding FFT power spectrum.

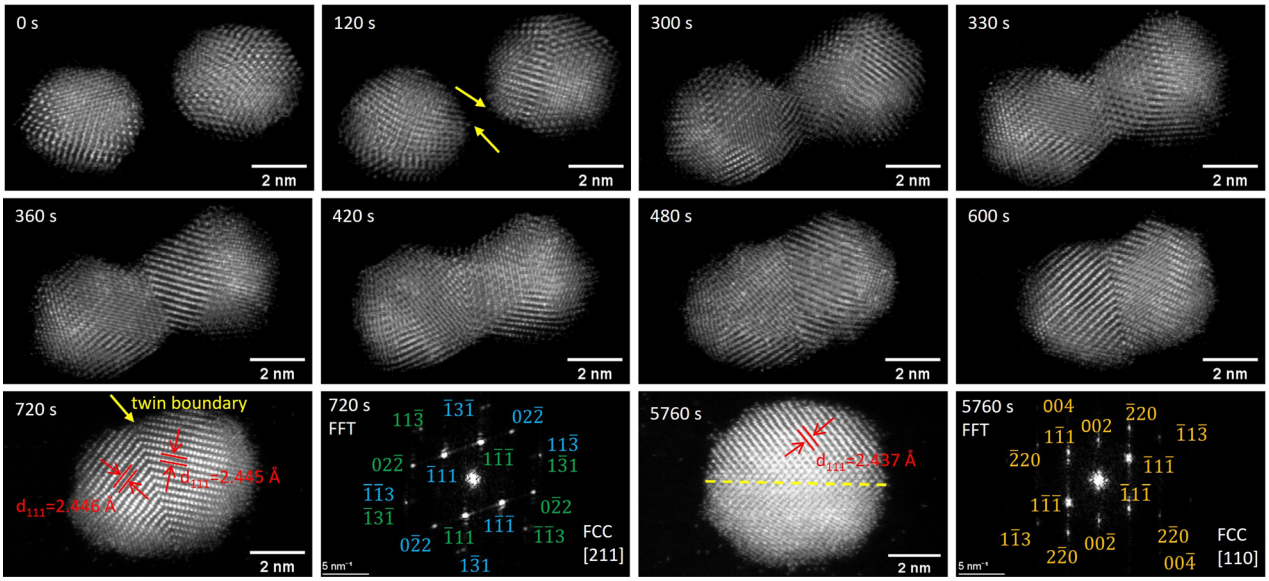

Fig. 2 Representative HAADF-STEM images of another pair of Au_{2057} clusters during the electron beam welding process along with the corresponding FFT power spectrum at 720 s and 5760 s. The arrows at 120 s indicate the precursors to the formation of the neck, and the arrow at 720 s indicates the formation of the twinned boundary.

and resulting in a smoother surface with no voids. At this stage, the movement of atoms induces the misorientation alignment, creating stress within the cluster. The oriented attachment process involves cluster rotation and grain boundary migration. As the process continues, the nanoclusters tend toward a more stable structure. As a result, atomic rearrangement occurs *via* the climb and slip of the misfit dislocation, displacing defects and releasing internal stresses. During the NW process, the neck generally forms {111} planes of clusters and operates as an atomic diffusion path for coalescence. Throughout these processes, there is a significant reduction in both the total surface energy and interface energy of the system, and some lattice distortions are eliminated. Notably, these processes can occur at temperatures far below the melting temperature of the corresponding bulk material.

Homogeneous EBW between oxidized Ta NCs

The effects of EBI on Ta_{10000} clusters were investigated in Fig. 3(a)–(g). The five clusters before and after EBI are labelled with blue and orange numbering 1–5, respectively. Herein, EBI was performed on cluster 3 at an electron dose of 1.31×10^7 e^- per nm^2 per frame for one hour, while the other clusters were not irradiated. The high-resolution HAADF-STEM images and corresponding FFT of cluster 3 before and after EBI are shown in insets (a) and (d) of Fig. 3. Furthermore, the EDS characterization was utilized to measure the Ta/O atomic ratio, as illustrated in Fig. 3(g). Orange circles and blue pentagrams represent the five clusters before and after EBI, respectively, and their labels align with the *x*-axis of the graph. Before EBI, Ta_{10000} exhibited an irregular amorphous structure with a metallic tantalum core covered by an oxidized amorphous shell. The EDS elemental mapping reveals significant enrichment of oxygen in the region where the Ta clusters are located. The Ta : O atomic ratio obtained through EDS characterization before EBI is found to be around 2 : 5, indicating that Ta predominantly exists in the +5 oxidation state. Ta clusters are prone to oxidation, forming loosely packed and amorphous structures, which is consistent with what has been reported in previous literature.[12] This behavior poses challenges for establishing accurate lattice matching at the interface, which presents a hurdle for EBW. However, it was found that the application of EBI transformed cluster 3 from an amorphous structure to a crystalline structure. Two rings in reciprocal space were observes in Fig. 3(d) inset, revealing the formation of an polycrystalline structure, and the corresponding interplanar distances are measured to be 2.56 Å and 1.32 Å, respectively. Furthermore, the EBI resulted in an increase in the Ta : O atomic ratio of cluster 3 from 2 : 5 to 1 : 1, as depicted in Fig. 3(g), while the ratio remains approximately 2 : 5 in other clusters. Fig. 3(h) depicts three adjacent Ta_{923} clusters, and Fig. 3(j) shows three linearly arranged Ta_{923} clusters. After EBI at electron dose of 3.87×10^6 e^- per nm^2 per frame and 1.55×10^6 e^- per nm^2 per frame respectively, electron beam NW processes were completed and the lattices at the cluster interface were automatically matched, as shown in Fig. 3(i) and (k) correspondingly. The rings in the FFTs indicate the formation of polycrystalline structures after welding.

During the aforementioned processes, EBI primarily resulted in three effects: (1) partial elimination of oxygen atoms, leading to a certain degree of de-oxidation; (2) transformation of oxidized Ta clusters from amorphous structure to crystalline structure; and (3) successful completion of the welding process for oxidized Ta clusters, forming a polycrystalline structure at the welded neck. These effects were mainly caused by elastic electron–atom scattering and inelastic electron–phonon scattering.[47]

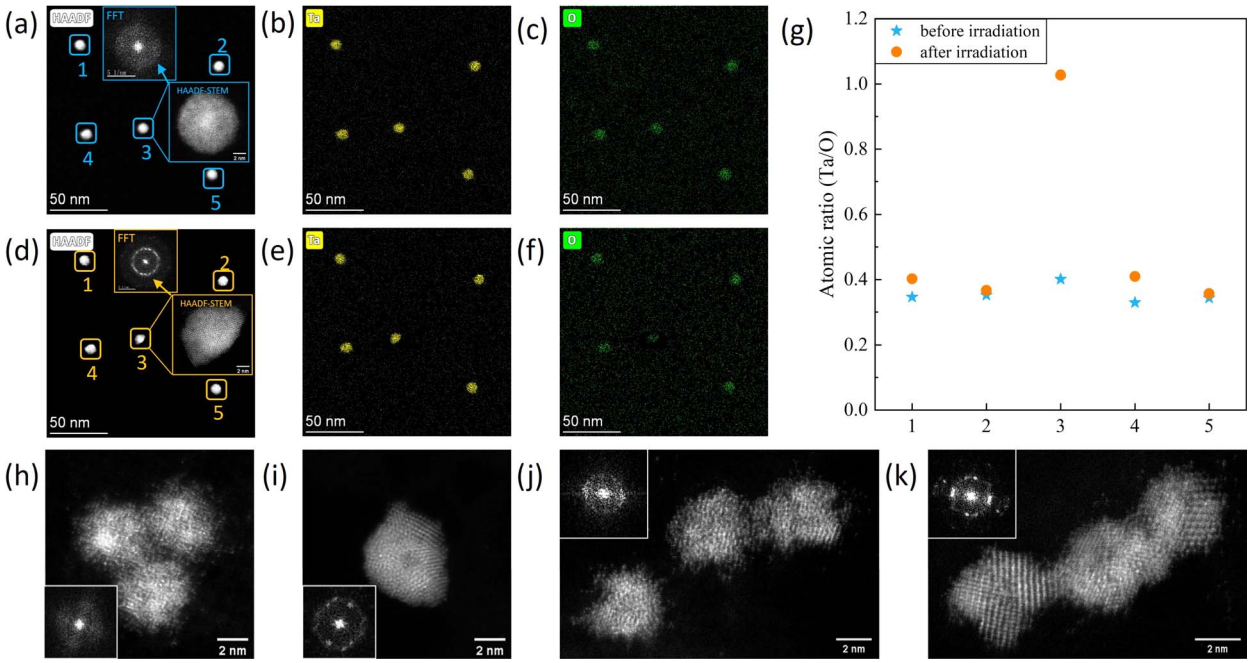

Fig. 3 Electron beam irradiation induced crystallization, partly de-oxidation, and nano-welding of oxidized tantalum clusters. The EDS characterization of Ta_{10000} cluster acquired before (a–c) and after (d–f) EBI are shown, respectively. (g) Changes in Ta/O atomic ratio of area 1–5 before (blue) and after (orange) EBI. (h) High-resolution HAADF-STEM image of three oxidized Ta_{923} clusters adjacent to each other before EBI. (i) High-resolution HAADF-STEM image of Ta_{2769} cluster formed from (h) after EBI. The electron beam nano-welding of three Ta_{923} clusters is shown in (j) and (k). The corresponding Fast Fourier Transforms (FFTs) are displayed in the insets of (h)–(k).

When high-energy electron beam undergoes elastic scattering with atomic nuclei in clusters, the transfer of momentum from electrons to atomic nuclei results in atomic displacement, also known as knock-on damage. This elastic scattering process adheres to the conservation laws of kinetic energy and momentum. The energy transferred from the electron to the atomic nucleus is given by:[48]

$$\Delta E = \frac{2ME(E+2mc^2)}{(M+m)^2c^2+2ME}\sin^2\frac{\theta}{2}$$

where ΔE is the energy transferred to the atomic nucleus, E is the kinetic energy of the incident electron, m is the mass of the electron, M is the mass of the atomic nucleus, c is the speed of light, and θ is the scattering angle of the electron. The equation above indicates that at higher electron beam energies, larger scattering angles, and lower atomic numbers, the kinetic energy transferred from the incident electron beam to the atomic nucleus is higher. In principle, if ΔE exceeds the threshold energy for the atomic displacement in the cluster, denoted as E_d, the collided atoms are likely to deviate from their original equilibrium positions. This atomic displacement process is irreversible and can accumulate over time. Nevertheless, the threshold energy for sputtering of surface atoms from the cluster, denoted as E_s, is significantly lower, approximately 1/2 to 1/5 of the corresponding E_d.[47] Consequently, surface atoms may detach from the cluster surface after the collision and become free atoms.

The highest energy transferred to tantalum (Ta) and oxygen (O) atoms in elastic collisions is 2.9 eV and 33 eV, respectively, with incident electron beam energy of 200 keV.[34] O exhibits a higher propensity for energy acquisition in inelastic collisions than Ta, and it possesses lower threshold energy for E_s and E_d. Consequently, the displacement scattering cross-section of O surpasses that of Ta significantly. Therefore, when subjected to an incident energy of 200 keV, a substantial number of O atoms were sputtered by the high-energy electron beam, dislodging from the cluster surface and entering the vacuum, thereby inducing partial deoxidation of the material. Furthermore, a small amount of Ta atoms is also sputtered out, entering the vacuum, or adhering to the carbon film substrate.

Phonons are quantized collective excitations in a periodic, elastic arrangement of atoms or molecules in condensed matter. They play a critical role in thermal conductivity and the transfer of heat within materials. When an electron beam interacts with a solid specimen, it can create phonons, transferring energy to the lattice and increasing the material's temperature. This process can occur even in amorphous solids, which lack a periodic crystal structure.[34] Phonon vibrations serve as a mechanism to convert the energy transferred from the electrons into the internal energy of the sample, resulting in heating effects. The heating effect of EBI is a complex process affected by three main factors: the total energy absorbed by the sample from inelastic electron–phonon scattering, the thermal conductivity of the sample, and the relaxation time of excited electrons. For metallic materials, heating effects are generally small. However, tantalum pentoxide (Ta_2O_5) has a very low thermal conductivity ($\sim$0.2–0.4 $W\,m^{-1}\,K^{-1}$) and a high electrical resistivity ($\sim10^{12}$ to 10^{14} Ω cm).[49,50] Therefore, significant

heating effects were caused by inelastic electron–phonon scattering within the oxidized Ta NCs. It is the primary intrinsic mechanism of EBI-induced crystallization. Amorphous structures are generally considered to be metastable, with a significant energy barrier between amorphous structures and crystalline structures. In contrast to crystalline structures such as Au NCs, the concentration of vacancies in amorphous structures is highly variable due to its nonequilibrium nature. The transition from an amorphous structure to a crystalline one requires overcoming a specific energy barrier associated with the activation energy required for diffusion. This transformation involves the reconstruction of atomic arrangements, where atoms in metastable states are activated by thermal energy and migrate towards positions with minimal energy.[12,51,52] Additionally, thermal stress induces the formation of dislocations during crystallization, typically resulting in a polycrystalline structure.

Furthermore, the underlying coalescence mechanism of the welding process shown in Fig. 3(h)–(k) is similar to that of Au clusters, where the fundamental driving force is the minimization of total surface energy, achieved *via* electron beam-driven surface atoms migration.

Heterogeneous EBW between Au–Ta NCs

Fig. 4(a)–(j) showcases EBW between two amorphous oxidized Ta_{561} clusters and an FCC-structured Au_{5083} cluster at an electron dose of 7.83×10^6 e^- per nm^2 per frame. The measured *d*-spacing of the Au_{5083} (111) crystal plane is 2.436 Å, slightly larger than the value (2.3548 Å) mentioned in the JCPDS PDF data #98-000-0230. Due to the heating effects induced by EBI, the Ta_{561} clusters gradually transformed from a loose amorphous structure to a dense crystalline structure. Interestingly, this structural transformation initiated at the interface between Ta_{561} and Au_{5083} and progressed layer by layer in an epitaxial crystallization manner. Additionally, during the structural relaxation process, the grain boundaries emerged in Au_{5083} due to structural competition. As the process continued, the migration of the grain boundary from the central position towards the periphery of the cluster resulted in the elimination of a portion of dislocations and stacking faults in the Au_{5083} cluster. By 1380 s, the lattice alignment between Ta_{561} and Au_{5083} clusters was perfect, forming an FCC single crystal structure through epitaxial crystallization. While the FCC structure is not present in bulk tantalum oxide. The inset in Fig. 4(j) shows the FFT pattern along the [110] zone axis direction, revealing a measured d_{111} value of approximately 2.441 Å. The presence of tails in the FFT pattern indicates the existence of a small amount of stacking faults in the welded cluster, with the maximum disorientation angle of the faults being approximately 22°. Fig. 4(k)–(n) illustrates the EBW process between distorted icosahedral Au_{923} and amorphous oxidized Ta_{923} clusters at an electron dose of 7.83×10^6 e^- per nm^2 per frame. In contrast to the epitaxial crystallization phenomena observed in Fig. 4(a)–(j), non-epitaxial crystallization and coalescence were observed during the welding of two clusters of similar sizes. By 300 s, a spherical welded Au–Ta cluster exhibiting a polycrystalline structure was formed, as shown in Fig. 4(n). The lattice spacing of this structure corresponds to 2.427 Å, as indicated by the FFT pattern.

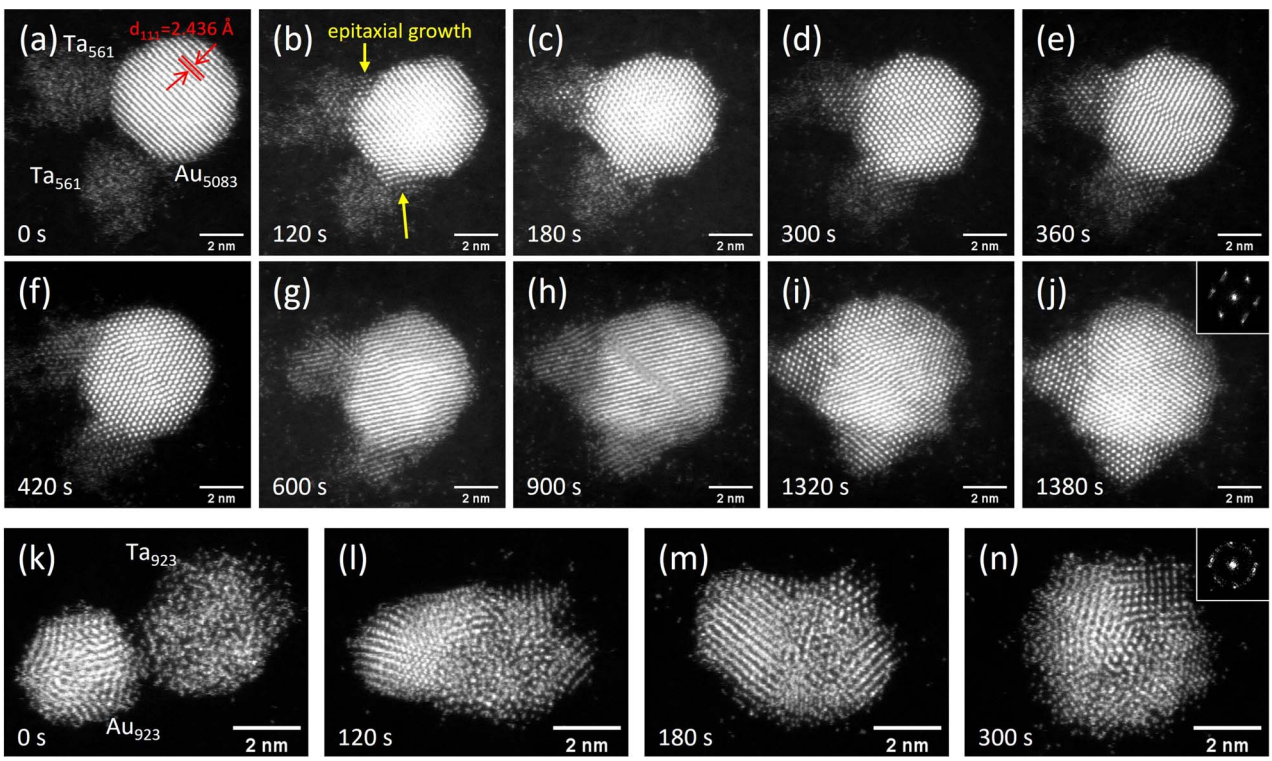

Fig. 4 (a–j) The EBW between two amorphous Ta_{561} clusters and one FCC-structured Au_{5083} cluster. (k–n) The EBW between distorted decahedral Au_{923} cluster and amorphous Ta_{923} cluster. The insets in (j) and (n) show the corresponding FFT power spectrum.

In the case of EBW shown in Fig. 4(a)–(j), the larger FCC-structured Au_{5083} cluster is stable enough to serve as a template for the amorphous Ta_{561} clusters to crystallize epitaxially. Consequently, the atoms within the Ta_{561} clusters arrange themselves in a manner that mirrors the FCC structure of the Au_{5083} clusters, resulting in a coherent FCC single-crystal structure. Eventually, a segregated interface with an FCC single-crystal structure was formed through epitaxial crystallization. In contrast, the non-epitaxial crystallization and coalescence behavior between distorted icosahedral Au_{923} and amorphous Ta_{923} clusters are due to the lack of a suitable crystallographic template and the irregular structure of the Au_{923} clusters. The atomic diffusion between Au and Ta atoms in the clusters resulted in the formation of solid solutions. Based on this, clusters can be utilized as intermediate fillers in EBW to address issues such as cracks and metallurgical incompatibility arising from differences in thermal and chemical properties between dissimilar materials. Furthermore, the clusters we prepared are size-selected, ensuring that clusters of the same size exhibit consistent thermodynamic properties. Therefore, we firmly believe that employing these size-selected clusters in welding processes will yield significantly enhanced mechanical and electrical properties compared to using non-uniform nanoparticles.

According to the literature, due to the significant disparity in both structure and thermal properties, EBW of bulk Au and Ta is widely acknowledged to possess a relatively low likelihood.[17,20,27] However, the present investigation revealed that Au and Ta clusters can be easily welded under EBI, forming single-crystal or polycrystalline structures. The EBW between immiscible materials is primarily limited by thermodynamic energy barriers. The Gibbs free energy of mixed systems for immiscible materials is given by:

$$\Delta G_{\mathrm{mix}} = \Delta H_{\mathrm{mix}} - T\Delta S_{\mathrm{mix}}$$

Here, ΔH_{mix} represents the mixing enthalpy, T represents the temperature, and ΔS_{mix} represents the mixing entropy. Welding can only be achieved when $\Delta G_{\mathrm{mix}} < 0$. Thus, low ΔH_{mix}, high T, and high ΔS_{mix} are favorable conditions for welding.

Due to the quantum size effect and surface effect, an additional negative term appears in mixing enthalpy ΔH_{mix}.[31,53] Given a bulk cohesive energy E_{b}, the cohesive energy E_n of a spherical nanocluster with n atoms can be expressed as:

$$E_n = E_{\mathrm{b}}\left(1 - \frac{1}{n^{1/3}}\right)$$

The bulk enthalpy of a single phase can be considered as the corresponding bulk cohesion energies, $H_{\mathrm{A}}^{\mathrm{bulk}} = E_{\mathrm{A}} < 0$ and $H_{\mathrm{B}}^{\mathrm{bulk}} = E_{\mathrm{B}} < 0$. The mixing enthalpy ΔH_{mix} and the mixing Gibbs energy ΔG_{mix} of an alloy nanocluster consisting of elements A and B can be written as:[31,53]

$$\begin{aligned}\Delta H_{\mathrm{mix}} &= H_{\mathrm{AB}} - x_{\mathrm{A}}H_{\mathrm{A}} - x_{\mathrm{B}}H_{\mathrm{B}} \\ &= \left(\Delta H_{\mathrm{mix}}^{\mathrm{bulk}} + x_{\mathrm{A}}H_{\mathrm{A}}^{\mathrm{bulk}} + x_{\mathrm{B}}H_{\mathrm{B}}^{\mathrm{bulk}}\right)\left(1 - \frac{1}{n^{1/3}}\right) \\ &\quad - x_{\mathrm{A}}H_{\mathrm{A}}^{\mathrm{bulk}}\left(1 - \frac{1}{n_{\mathrm{A}}{}^{1/3}}\right) - x_{\mathrm{B}}H_{\mathrm{B}}^{\mathrm{bulk}}\left(1 - \frac{1}{n_{\mathrm{B}}{}^{1/3}}\right)\end{aligned}$$

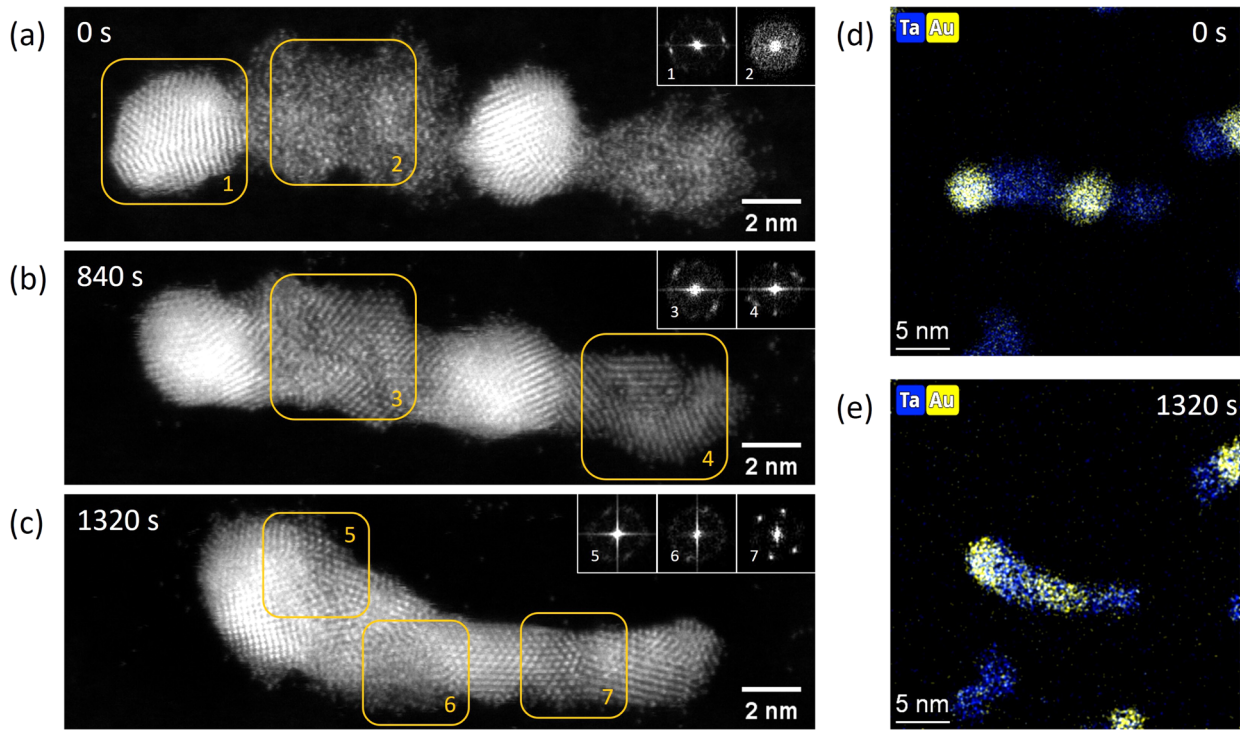

Fig. 5 (a–c) Electron beam welding of Au_{923}–Ta_{923}–Ta_{923}–Au_{923}–Ta_{923} chain of clusters. The corresponding EDS elemental mappings are shown in (d) and (e) respectively.

$$\Delta G_{mix} = \Delta H_{mix}^{bulk} - \frac{1}{n^{1/3}}\left[\Delta H_{mix}^{bulk} - H_A^{bulk}\left({x_A}^{2/3} - x_A\right) - H_B^{bulk}\left({x_B}^{2/3} - x_B\right)\right] + RT[x_A \ln(x_A) + x_B \ln(x_B)]$$

Here, n represents the number of atoms in the immiscible materials system, x_A and x_B are the corresponding atomic fractions of elements A and B. Due to the quantum size effect and surface effect, an additional negative term emerges. As n is small enough, ΔG_{mix} will decrease to a negative value, allowing for the formation of a stable crystalline structure at the welding interface. Additionally, the inelastic electron–phonon scattering-induced heating effect provides a higher temperature. Upon completion of the welding process, the combined system typically exhibits a positive mixing entropy ΔS_{mix}, further enhancing its thermodynamic stability.

Fig. 5(a)–(c) illustrates the EBW of a chain of clusters: Au_{923}–Ta_{923}–Ta_{923}–Au_{923}–Ta_{923} at an electron dose of 1.31×10^7 e^- per nm^2 per frame. Initially, at $t = 0$ s, the five clusters from left to right were decahedral Au_{923}, amorphous Ta_{923}, amorphous Ta_{923}, decahedral Au_{923}, and amorphous Ta_{923}, with clear boundaries between the clusters. At $t = 840$ s, due to the heating effect caused by electron–phonon interactions, the Ta_{923} clusters transformed from their initial loose amorphous structure into a dense crystalline structure. The corresponding FFT patterns are shown in the insets of the top right corners. During this process, the lattices of Au_{923} and Ta_{923} automatically matched, forming distinct grain boundaries. At $t = 1320$ s, driven by the high-energy electron beam, further diffusion occurred between Au and Ta atoms. The five clusters were welded together to form a continuous chain of clusters. The FFT analysis indicates that the boundaries between Au_{923} and Ta_{923} transitioned into a sintered necks with polycrystalline structures. Fig. 5(d) and (e) shows the EDS characterization before and after EBW. Before welding, the Au and Ta atoms were located in their respective Au_{923} and Ta_{923} positions. After the welding process, significant diffusion occurred at the boundaries between Au_{923} and Ta_{923}, forming a solid polycrystalline structure. The EDS mapping reveals the spatial distribution of elements, providing evidence for the formation of Au–Ta solid solutions. However, the elemental distribution is not uniform, indicating that the welded clusters are not homogeneous alloys.

Conclusions

The nano-welding of clusters under electron beam irradiation represents an intriguing frontier. This research comprehensively investigated the electron beam nano-welding process of size-selected Au and Ta nanoclusters *via in situ* aberration-corrected scanning transmission electron microscopy (AC-STEM), revealing the intrinsic mechanisms involved. The primary driving force behind the welding process is the reduction of excess surface energy. The application of high-energy electron beams introduces energy disruption to the system, resulting in the thermal migration of surface atoms. This phenomenon leads to the growth of sintering necks at the interfaces of adjacent clusters, where surface diffusion and recrystallization facilitate shape modification while maintaining stable facet planes. During this process, certain lattice distortions can be eliminated. However, there is competition in the structural orientation of internal atoms, ultimately resulting in the formation of either single-crystalline or polycrystalline structures. The knock-on damage caused by elastic scattering of the electron beam was observed to partially deoxidize the clusters. Additionally, the thermal effect induced by inelastic electron–phonon scattering facilitated the transformation of the oxidized Ta clusters from metastable amorphous structures to stable crystalline structures. Furthermore, considering the quantum size effect and surface effect of the clusters, these factors enabled successful electron beam nano-welding by surpassing the miscibility limits of bulk materials during Au–Ta heterogeneous welding processes. Our investigation contributes to a deeper comprehension of electron beam nano-welding phenomena. By bridging the gap between fundamental research on nanoclusters and their practical applications, our investigation of electron beam nano-welding represents a crucial stride towards advancing bottom-up atomic manufacturing, high-temperature power chip packaging, nano-device integration, 3D nano printing, and other related fields in the future.

Data availability

The data that support the findings of this study are available upon reasonable request from the authors.

Author contributions

Shengyong Hu: conceptualization, data curation, formal analysis, investigation, methodology, writing – original draft, writing – review & editing. Syed Adil Shah: conceptualization, data curation, formal analysis, investigation, methodology, writing – review & editing. Syed Niaz Ali Shah: investigation, writing – review & editing. Zixiang Zhao: data curation. Wuwen Zhu: investigation. Yongxin Zhang: investigation. Siqi Lu: formal analysis. Sichen Tang: investigation. Kuo-Juei Hu: supervision, resources, writing – review & editing. Fengqi Song: project administration, funding acquisition, resources, writing – review & editing.

Conflicts of interest

The authors declare that they have no known competing financial interests or personal relationships that could have appeared to influence the work reported in this paper.

Acknowledgements

We acknowledge the financial support of the National Key R&D Program of China (Grant No. 2022YFA1402404), the National Natural Science Foundation of China (Grant No. 92161201, T2221003, 92261204, 12104221, 12104220, 91961101, 12025404, 12004174, 62274085, 12274208, and 12274337), the Natural Science Foundation of Jiangsu Province (Grant No. BK20200312

and BK20200310), and the Fundamental Research Funds for the Central Universities (Grant No. 020414380192).

References

1 A. Sharif, N. Farid and G. M. O'Connor, Ultrashort laser sintering of metal nanoparticles: a review, *Results Eng.*, 2022, **16**, 100731.
2 J. Li, J. Chen, H. Wang, N. Chen, Z. Wang, L. Guo and F. L. Deepak, In Situ Atomic-Scale Study of Particle-Mediated Nucleation and Growth in Amorphous Bismuth to Nanocrystal Phase Transformation, *Adv. Sci.*, 2018, **5**, 1700992.
3 L. Li, M. Hong, M. Schmidt, M. Zhong, A. Malshe, B. Huis in't Veld and V. Kovalenko, Laser nano-manufacturing – state of the art and challenges, *CIRP Ann.*, 2011, **60**, 735–755.
4 J. Ji, Z. Zhou, X. Yang, W. Zhang, S. Sang and P. Li, One-dimensional nano-interconnection formation, *Small*, 2013, **9**, 3014–3029.
5 X. Liu, Z. Zheng, C. Wang, W. Liu, R. An and W. Zhang, Fusion behaviour and mechanism of ultrafine Ag-Cu nanoparticles induced by electron beam irradiation, *J. Mater. Sci.: Mater. Electron.*, 2017, **28**, 8206–8210.
6 L. Cheng, X. Zhu and J. Su, Coalescence between Au nanoparticles as induced by nanocurvature effect and electron beam athermal activation effect, *Nanoscale*, 2018, **10**, 7978–7983.
7 H. Ye, Z. Zhang and R. Wang, Nucleation and Growth of Nanocrystals Investigated by In Situ Transmission Electron Microscopy, *Small*, 2023, **19**, e2303872.
8 Z. Liu, Z. Wu, Q. Yao, Y. Cao, O. J. H. Chai and J. Xie, Correlations between the fundamentals and applications of ultrasmall metal nanoclusters: Recent advances in catalysis and biomedical applications, *Nano Today*, 2021, **36**, 101053.
9 H. Hassan, P. Sharma, M. R. Hasan, S. Singh, D. Thakur and J. Narang, Gold nanomaterials – the golden approach from synthesis to applications, *Mater. Sci. Energy Technol.*, 2022, **5**, 375–390.
10 S. A. Shah, K.-J. Hu, M. Naveed, C. Lu and S. Hu, Synthesis and study of the quantum-confinement effect of gold-nanoclusters via optical properties protected by 2-phenylethanethiol ligand, *Chem. Phys. Lett.*, 2023, **811**, 140206.
11 N. Patra, N. A. Nasiri, S. Grasso, D. J. Daniel and W. E. Lee, Green synthesis of nanosized Tantalum carbide (TaC) via natural polymer/tantalum oxide hybrid composites: a sustainable approach towards enhanced processing and properties, *J. Anal. Appl. Pyrolysis*, 2024, **179**, 106464.
12 S. Hu, K.-J. Hu, Y. Zhang, S. A. Shah, Z. Zhao, Z. Zuo, S. Lu, S. Tang, W. Zhu and L. Fang, Oxidation behavior and atomic structural transition of size-selected coalescence-resistant tantalum nanoclusters, *Nanotechnology*, 2024, **35**(31), 315603.
13 I. G. Akande, O. O. Oluwole, O. Fayomi and O. A. Odunlami, Overview of mechanical, microstructural, oxidation properties and high-temperature applications of superalloys, *Mater. Today: Proc.*, 2021, **43**, 2222–2231.
14 A. Kracke, Superalloys, the most successful alloy system of modern times-past, present and future, *Proceedings of the 7th International Symposium on Superalloy*, ed. E. A. Ott, J. R. Groh, A. Banik, I. Dempster, T. P. Gabb, R. Helmink, X. Liu, A. Mitchell, G. P. Sjöberg and A. Wusatowska-Sarnek, 2010, vol. 718, pp. 13–50.
15 G. Çam and M. Koçak, Progress in joining of advanced materials, *Int. Mater. Rev.*, 1998, **43**, 1–44.
16 J. P. Oliveira, T. G. Santos and R. M. Miranda, Revisiting fundamental welding concepts to improve additive manufacturing: from theory to practice, *Prog. Mater. Sci.*, 2020, **107**, 100590.
17 M. Węglowski, S. Błacha and A. Phillips, Electron beam welding – techniques and trends – review, *Vacuum*, 2016, **130**, 72–92.
18 P. Lacki, K. Adamus and P. Wieczorek, Theoretical and experimental analysis of thermo-mechanical phenomena during electron beam welding process, *Comput. Mater. Sci.*, 2014, **94**, 17–26.
19 I. G. Gonzalez-Martinez, A. Bachmatiuk, V. Bezugly, J. Kunstmann, T. Gemming, Z. Liu, G. Cuniberti and M. H. Rümmeli, Electron-beam induced synthesis of nanostructures: a review, *Nanoscale*, 2016, **8**, 11340–11362.
20 Z. Sun and R. Karppi, The application of electron beam welding for the joining of dissimilar metals: an overview, *J. Mater. Process. Technol.*, 1996, **59**, 257–267.
21 Y. Dai, P. Lu, Z. Cao, C. T. Campbell and Y. Xia, The physical chemistry and materials science behind sinter-resistant catalysts, *Chem. Soc. Rev.*, 2018, **47**, 4314–4331.
22 M. José-Yacaman, C. Gutierrez-Wing, M. Miki, D.-Q. Yang, K. N. Piyakis and E. Sacher, Surface diffusion and coalescence of mobile metal nanoparticles, *J. Phys. Chem. B*, 2005, **109**, 9703–9711.
23 I. Tomashchuk, P. Sallamand, N. Belyavina and M. Pilloz, Evolution of microstructures and mechanical properties during dissimilar electron beam welding of titanium alloy to stainless steel via copper interlayer, *Mater. Sci. Eng., A*, 2013, **585**, 114–122.
24 G. Liu, S. Yang, J. Ding, W. Han, L. Zhou, M. Zhang, S. Zhou, R. Misra, F. Wan and C. Shang, Formation and evolution of layered structure in dissimilar welded joints between ferritic-martensitic steel and 316L stainless steel with fillers, *J. Mater. Sci. Technol.*, 2019, **35**, 2665–2681.
25 W. Huang, W. Cai, T. J. Rinker, J. Bracey and W. Tan, Effects of laser oscillation on metal mixing, microstructure, and mechanical property of aluminum–copper welds, *Int. J. Mach. Tool Manufact.*, 2023, **188**, 104020.
26 T. Wang, B. Zhang, G. Chen and J. Feng, High strength electron beam welded titanium–stainless steel joint with V/Cu based composite filler metals, *Vacuum*, 2013, **94**, 41–47.
27 K. Martinsen, S. J. Hu and B. E. Carlson, Joining of dissimilar materials, *CIRP Ann.*, 2015, **64**, 679–699.
28 P. Meakin, T. Vicsek and F. Family, Dynamic cluster-size distribution in cluster-cluster aggregation: effects of cluster diffusivity, *Phys. Rev. B: Condens. Matter Mater. Phys.*, 1985, **31**, 564–569.

29 L. J. Lewis, P. Jensen and J.-L. Barrat, Melting, freezing, and coalescence of gold nanoclusters, *Phys. Rev. B: Condens. Matter Mater. Phys.*, 1997, **56**, 2248–2257.
30 P. Peng, A. Hu, A. P. Gerlich, G. Zou, L. Liu and Y. N. Zhou, Joining of Silver Nanomaterials at Low Temperatures: Processes, Properties, and Applications, *ACS Appl. Mater. Interfaces*, 2015, **7**, 12597–12618.
31 J. Feng, D. Chen, P. V. Pikhitsa, Y. Jung, J. Yang and M. Choi, Unconventional Alloys Confined in Nanoparticles: Building Blocks for New Matter, *Matter*, 2020, **3**, 1646–1663.
32 J. Yan, G. Zou, Y. Zhang, J. Li, L. Liu, A. Wu and Y. N. Zhou, Metal–Metal Bonding Process Using Cu+Ag Mixed Nanoparticles, *Mater. Trans.*, 2013, **54**, 879–883.
33 L. Yin, F. Yang, X. Bao, W. Xue, Z. Du, X. Wang, J. Cheng, H. Ji, J. Sui, X. Liu, Y. Wang, F. Cao, J. Mao, M. Li, Z. Ren and Q. Zhang, Low-temperature sintering of Ag nanoparticles for high-performance thermoelectric module design, *Nat. Energy*, 2023, **8**, 665–674.
34 D. B. Williams and C. B. Carter, *Transmission electron microscopy. A textbook for materials science*, Springer, New York, 2nd edn, 2008.
35 S. Jaypuria, V. Bondada, S. Kumar Gupta, D. Kumar Pratihar, D. Chakrabarti and M. N. Jha, Prediction of electron beam weld quality from weld bead surface using clustering and support vector regression, *Expert Syst. Appl.*, 2023, **211**, 118677.
36 J. M. Yuk, M. Jeong, S. Y. Kim, H. K. Seo, J. Kim and J. Y. Lee, In situ atomic imaging of coalescence of Au nanoparticles on graphene: rotation and grain boundary migration, *Chem. Commun.*, 2013, **49**, 11479–11481.
37 Y. Peng, T. Cullis and B. Inkson, Bottom-up nanoconstruction by the welding of individual metallic nanoobjects using nanoscale solder, *Nano Lett.*, 2009, **9**, 91–96.
38 D. Nelli, G. Rossi, Z. Wang, R. E. Palmer and R. Ferrando, Structure and orientation effects in the coalescence of Au clusters, *Nanoscale*, 2020, **12**, 7688–7699.
39 D. V. Wagle and G. A. Baker, Cold welding: a phenomenon for spontaneous self-healing and shape genesis at the nanoscale, *Mater. Horiz.*, 2015, **2**, 157–167.
40 M. Ding, D. C. Sorescu, G. P. Kotchey and A. Star, Welding of gold nanoparticles on graphitic templates for chemical sensing, *J. Am. Chem. Soc.*, 2012, **134**, 3472–3479.
41 Z.-J. Zhao, S.-H. Shin, D.-G. Choi, S.-H. Park and J.-H. Jeong, Shape-Controlled 3D Periodic Metal Nanostructures Fabricated via Nanowelding, *Small*, 2018, **14**(6), 1703102.
42 D. N. Madsen, K. Mølhave, R. Mateiu, A. M. Rasmussen, M. Brorson, C. J. H. Jacobsen and P. Bøggild, Soldering of Nanotubes onto Microelectrodes, *Nano Lett.*, 2003, **3**, 47–49.
43 S. C. Laza, N. Sanson, C. Sicard-Roselli, A. Aghedu and B. Palpant, Selective Cold Welding of Colloidal Gold Nanorods, *Part. Part. Syst. Charact.*, 2013, **30**, 584–589.
44 E. C. Garnett, W. Cai, J. J. Cha, F. Mahmood, S. T. Connor, M. Greyson Christoforo, Y. Cui, M. D. McGehee and M. L. Brongersma, Self-limited plasmonic welding of silver nanowire junctions, *Nat. Mater.*, 2012, **11**, 241–249.
45 S. J. Barcelo, A. Kim, W. Wu and Z. Li, Fabrication of deterministic nanostructure assemblies with sub-nanometer spacing using a nanoimprinting transfer technique, *ACS Nano*, 2012, **6**, 6446–6452.
46 S.-H. Cha, S.-H. Kang, Y. J. Lee, J.-H. Kim, E.-Y. Ahn, Y. Park and S. Cho, Fabrication of nanoribbons by dielectrophoresis assisted cold welding of gold nanoparticles on mica substrate, *Sci. Rep.*, 2019, **9**, 3629.
47 N. Jiang, Electron beam damage in oxides: a review, *Rep. Prog. Phys.*, 2016, **79**, 16501.
48 D. Knez, M. Schnedlitz, M. Lasserus, A. Schiffmann, W. E. Ernst and F. Hofer, Modelling electron beam induced dynamics in metallic nanoclusters, *Ultramicroscopy*, 2018, **192**, 69–79.
49 M. C. Gurak, Studies of the Yttrium Tantalate – Zirconium Oxide Quasi-Binary, PhD thesis, Harvard University, 2017.
50 P. Xu, *Investigation of the Thermal Transport in Superconducting Niobium and Tantalum*, Michigan State University, 2019.
51 K. A. Jackson, *Kinetic processes: crystal growth, diffusion, and phase transitions in materials*, John Wiley & Sons, 2010.
52 C. Bhugra and M. J. Pikal, Role of thermodynamic, molecular, and kinetic factors in crystallization from the amorphous state, *J. Pharm. Sci.*, 2008, **97**, 1329–1349.
53 J. M. La Martinez De Hoz, R. Callejas Tovar and P. B. Balbuena, Size effect on the stability of Cu–Ag nanoalloys, *Mol. Simul.*, 2009, **35**, 785–794.